NANO LETTERS

May 2019
Volume 19, Number 5
pubs.acs.org/NanoLett

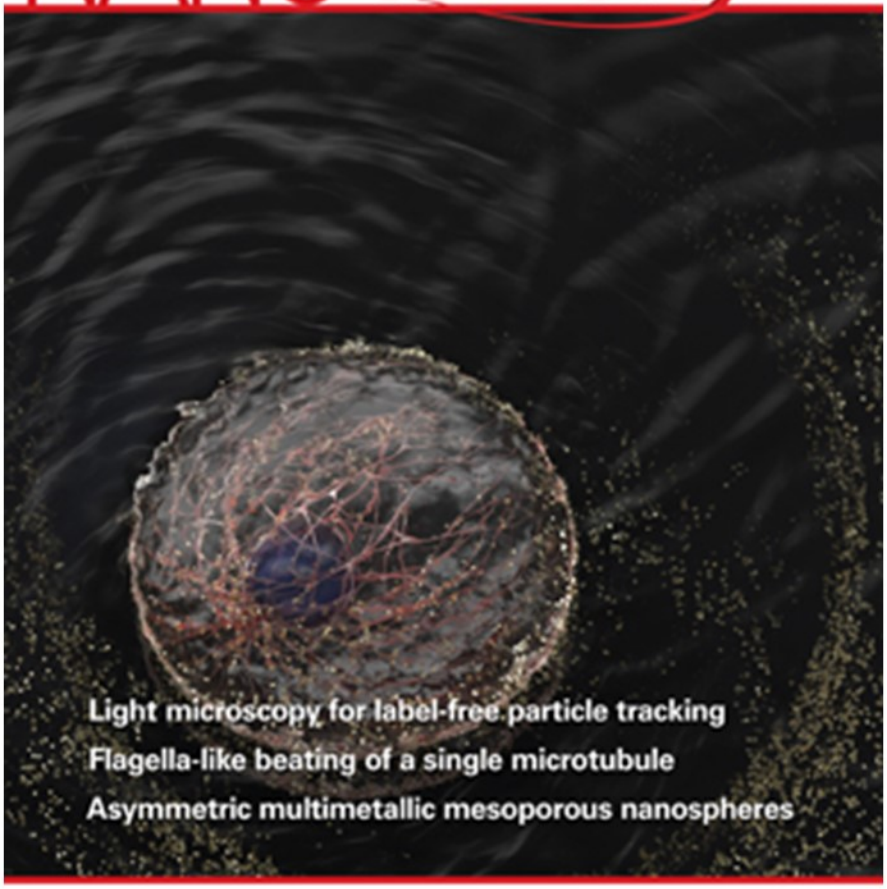

Light microscopy for label-free particle tracking

Flagella-like beating of a single microtubule

Asymmetric multimetallic mesoporous nanospheres

ACS Publications
Most Trusted. Most Cited. Most Read.

www.acs.org

NANO LETTERS
Letter
Cite This: Nano Lett. 2019, 19, 793−804
pubs.acs.org/NanoLett

Scatter Enhanced Phase Contrast Microscopy for Discriminating Mechanisms of Active Nanoparticle Transport in Living Cells

John F. Zimmerman,[†] Herdeline Ann M. Ardoña,[†] Georgios Pyrgiotakis,[‡] Jiaqi Dong,[§] Brij Moudgil,[§] Philip Demokritou,[‡] and Kevin Kit Parker*[,†]

[†]Disease Biophysics Group, John A. Paulson School of Engineering and Applied Sciences, Wyss Institute for Biologically Inspired Engineering, Harvard University, Cambridge, Massachusetts 02452, United States

[‡]Center for Nanotechnology and Nanotoxicology, Harvard T.H. Chan School of Public Health, Harvard University, Cambridge, Massachusetts 02138, United States

[§]Department of Materials Science & Engineering and Particle Engineering Research Center, University of Florida, P.O. Box 116135, Gainesville, Florida 32611, United States

Supporting Information

ABSTRACT: Understanding the uptake and transport dynamics of engineered nanomaterials (ENMs) by mammalian cells is an important step in designing next-generation drug delivery systems. However, to track these materials and their cellular interactions, current studies often depend on surface-bound fluorescent labels, which have the potential to alter native cellular recognition events. As a result, there is still a need to develop methods capable of monitoring ENM-cell interactions independent of surface modification. Addressing these concerns, here we show how scatter enhanced phase contrast (SEPC) microscopy can be extended to work as a generalized label-free approach for monitoring nanoparticle uptake and transport dynamics. To determine which materials can be studied using SEPC, we turn to Lorenz−Mie theory, which predicts that individual particles down to ∼35 nm can be observed. We confirm this experimentally, demonstrating that SEPC works for a variety of metal and metal oxides, including Au, Ag, TiO_2, CeO_2, Al_2O_3, and Fe_2O_3 nanoparticles. We then demonstrate that SEPC microscopy can be used in a quantitative, time-dependent fashion to discriminate between distinct modes of active cellular transport, including intracellular transport and membrane-assisted transport. Finally, we combine this technique with microcontact printing to normalize transport dynamics across multiple cells, allowing for a careful study of ensemble TiO_2 nanoparticle uptake. This revealed three distinct regions of particle transport across the cell, indicating that membrane dynamics play an important role in regulating particle flow. By avoiding fluorescent labels, SEPC allows for a rational exploration of the surface properties of nanomaterials in their native state and their role in endocytosis and cellular transport.

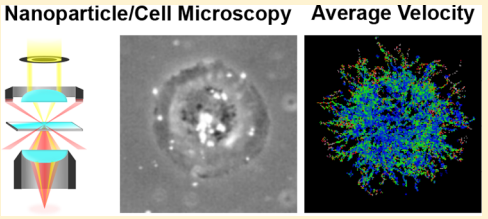

KEYWORDS: *Scatter enhanced phase contrast, endocytosis, nanoparticle, Lorenz−Mie theory, nano-bio interface*

Engineered nanomaterials (ENMs) have emerged as an important class of materials for use in biology and medicine, due to their unique size- and shape-dependent chemical, mechanical, and physical properties.[1,2] This allows ENMs to be introduced in a drug-like fashion, with potential applications as bio-orthogonal therapeutic devices and as vehicles for drug delivery.[3−6] However, as nanostructured materials have begun to see broader laboratory and commercial use, there is still a great need for understanding how these materials are internalized and distributed at cellular length scales. This is important for assessing the impact of existing ENM pollutants on human health and physiology, and for rationally controlling the mechanism of nanoparticle uptake. In this regard, nanomaterials have been reported to be internalized through a number of different receptor-mediated pathways,[7] including clathrin-[8−10] and dynamin[11−13]-dependent endocytosis. However, predicting a priori if an ENM will be internalized, and by what mechanism, is still challenging as chemical composition, size, shape, and surface properties all play a significant role in mediating ENM endocytosis.[10,14,15]

In particular, isolating the role of surface modifications represents a significant challenge, as methods for studying ENM uptake and toxicity have traditionally depended on fluorescent markers for use in nanoparticle (NP) tracking.[16−18] This can be problematic, as fluorescent labels can change the existing hydrodynamic radius and surface potential of a material, both of which have an impact NP endocytosis.[15,19,20] Second, fluorescent labels can be toxic, making it difficult to distinguish between intrinsic NP cytotoxicity and the effects of surface coatings. Finally, the use of fluorescent labels can interfere with native protein corona formation and particle opsonization, further impacting downstream particle uptake.[20] While this does not prohibit the study of inherently fluorescent

Received: September 27, 2018
Revised: December 20, 2018
Published: January 7, 2019

Downloaded via HARVARD UNIV on December 8, 2020 at 22:17:32 (UTC).
See https://pubs.acs.org/sharingguidelines for options on how to legitimately share published articles.

© 2019 American Chemical Society

DOI: 10.1021/acs.nanolett.8b03903
Nano Lett. 2019, 19, 793−804

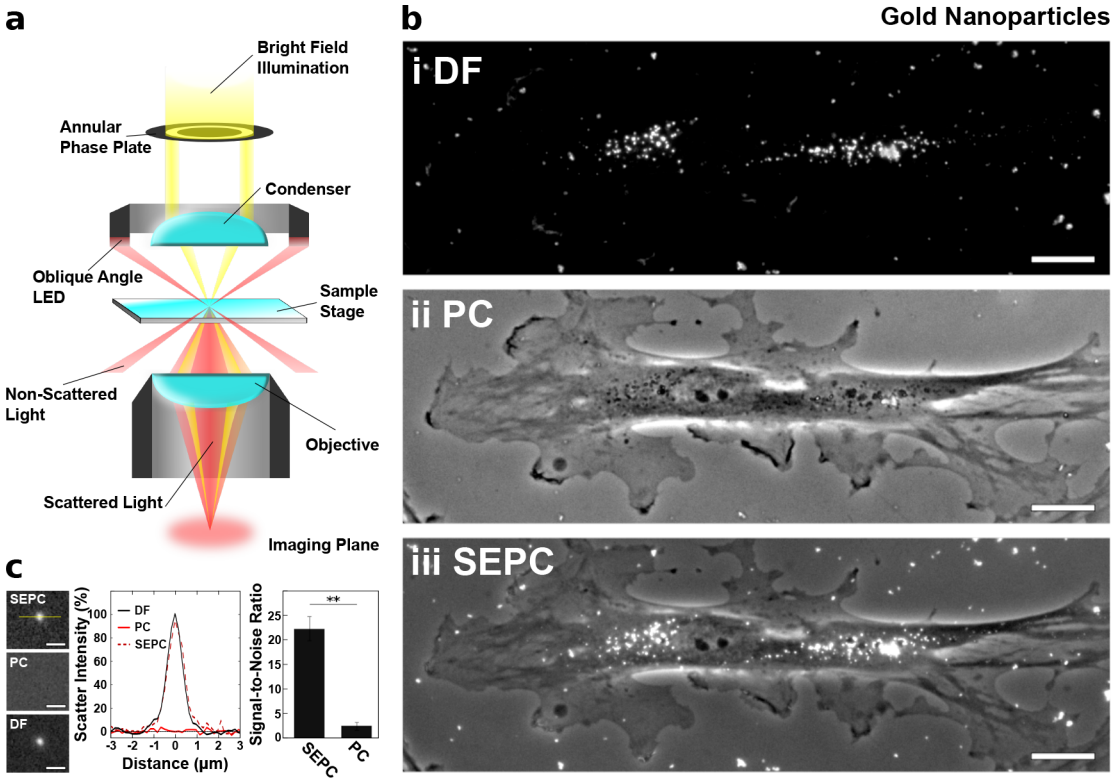

Figure 1. Scatter enhanced phase contrast (SEPC) allowing the simultaneous visualization of cells and ENMs. (a) SEPC light path diagram, illustrating a two-light source approach. (b) Example micrographs of HUVECs, which have been exposed to AuNPs. Micrographs obtained using darkfield (DF) (b, i), phase contrast (PC) (b, ii), and SEPC (b, iii) microscopy (scale bars, 20 μm). (c) Line plot indicating the normalized signal intensity of each microscopy method for AuNP taken along the highlighted region. Corresponding signal-to-noise ratio measurements for SEPC and PC imaging modes using DF as a reference (n = 13 444 particles over 11 fields of view), indicating a marked increase in the signal-to-noise ratio.

materials, it creates a challenge in addressing the broader range of available NPs, such as metals and metal oxides, which are among the most commonly produced nanomaterials.[21] However, understanding these mechanisms of endocytosis and intracellular trafficking are essential for rationally engineering the delivery of NPs and in understanding the physiological impacts of existing materials. As a result, there is still a need to develop improved label-free methods capable of tracking ENMs in a real-time manner without the use of an additional surface modification.

To address these concerns, here we show how scatter enhanced phase contrast (SEPC) can be used as a generalized approach for monitoring ENM endocytosis and particle transport. SEPC is an optical microscopy technique, which allows for the simultaneous visualization of both cells and nanomaterials in a label-free manner. Previously reported in the context silicon nanowires,[22] here we show how this method can be extended to smaller particles, whose largest dimensions are less than 100 nm. This allows for the visualization of a range of metals and metal oxides ENMs. To understand the limits of this system, we use the Lorenz−Mie theory as an accessible approach for understanding NP optical scattering, providing a theoretical framework for determining which particles can be tracked using SEPC. To validate this approach, we show that SEPC microscopy can be correlated to hyperspectral darkfield imaging and Raman spectroscopy, allowing for an independent assessment of ENM identity. We then demonstrate that SEPC can be used to track the real-time dynamics of ENM endocytosis across multiple particles compositions and cells types. Finally, combining this technique with microcontact printing, we demonstrate how SEPC can be used to study the normalized uptake of ENMs. Examining titanium oxide (TiO_2) NP endocytosis, we observe three distinct regions of transport, with particles exhibiting perinuclear clustering and spatially heterogeneous transport velocities. Collectively, this makes SEPC microscopy a powerful tool for understanding ENM-cell dynamics, providing insights into using nanomaterials as drug delivery systems and in understanding the environmental risk factors associated with existing ENMs.

SEPC Microscopy. SEPC allows for the simultaneous visualization of both cells and nanomaterials in a label-free manner by combining two traditional microscopy techniques: darkfield (DF) and phase contrast (PC) microscopy (Figure 1a). Due to the difference in optical properties between NPs and cells, it is usually challenging to track both at the same time using a single approach. Inorganic NPs typically possess a high refractive index, scattering light readily, making them easily discerned with DF microscopy. However, the subdiffraction length scale of inorganic NPs makes them difficult to observe using brightfield techniques. Conversely, while adherent cells are difficult to visualize under DF because of their low refractive index, they can be tracked using brightfield techniques such as PC and differential interference contrast (DIC), both of which can provide high fidelity cellular imaging (Figure S1). In traditional optical microscopy, both PC and DF condensers occupy the same position in the light path. This configuration limits the minimum achievable acquisition

DOI: 10.1021/acs.nanolett.8b03903
Nano Lett. 2019, 19, 793−804

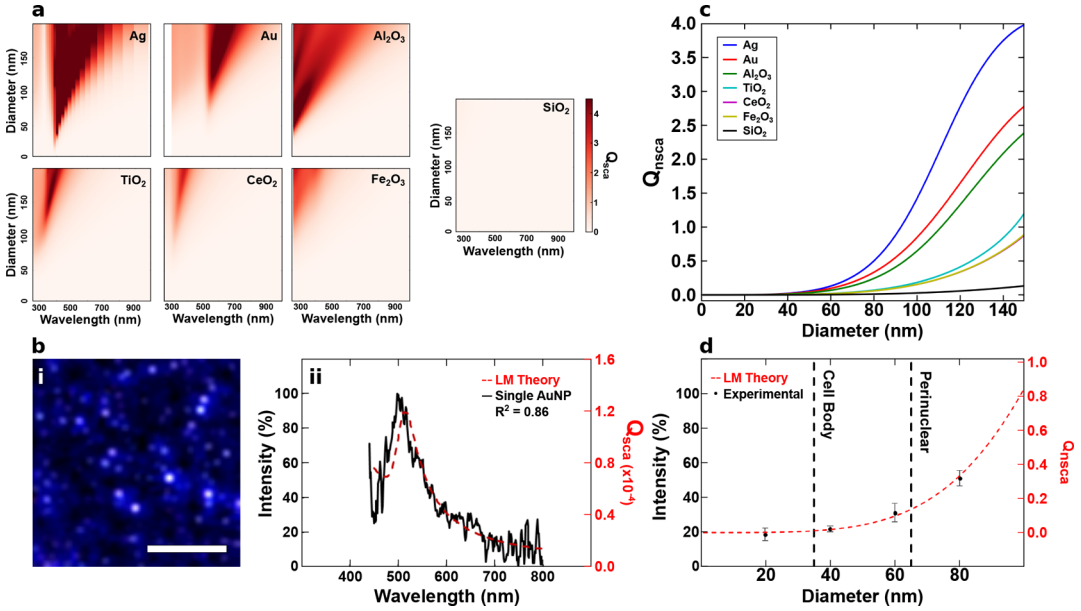

Figure 2. Lorenz−Mie theory model of particle DF scattering, predicting which particles can be viewed using SEPC. (a) Calculated scattering efficiency (Q_{sca}) of example inorganic NPs. (b) Hyperspectral micrograph of AuNPs (scale bar, 5 μm)(b, i), with the corresponding single particle scattering profile (12 nm, black) (b, ii) which agrees with LM theory predicted scattering spectrum (red) (R^2 = 0.86). Images were contrast adjusted and smoothed for clarity. (c) Predicted NP scattering was normalized across the wavelength-dependent illumination intensity and camera recording sensitivity. (d) Comparison of optical scattering intensities predicted by Lorenz−Mie theory (red) and recorded experimentally (black) for AuNPs of varying sizes, showing a good fit between theory and observation (3 s exposure time). Error bars given as the standard deviation.

interval, as condenser changeover and recalibration both require additional time, making it difficult to acquire real-time images in this manner. Here, we show how SEPC microscopy can bridge this gap by combining two-light sources to physically superimpose DF and PC images, giving SEPC microscopy the potential to track both cells and ENMs simultaneously.

To demonstrate this approach, gold nanoparticles (AuNPs) (18 nm diameter, Figure S2, Table S2) were incubated with human umbilical vascular endothelial cells (HUVECs) and imaged under DF, PC, and SEPC (Figure 1b). As expected, this showed that NPs could be readily visualized under DF (Figure 1b, i), while cells were apparent under PC (Figure 1b, ii). Next, when combining each technique using SEPC, both cells and ENM could be distinctly recognized (Figure 1b, iii). Using SEPC microscopy in this way means that ENMs can be placed in the context of the cell, in contrast to DF and PC techniques, which primarily focus on these individual components separately. This allows for a better visualization of the interactions of ENMs with cellular systems. To quantify this, DF was used as an experimental control for NP location, and particle signal intensity was measured relative to the background intensity in each imaging mode. Using AuNPs as a control for signal intensity, SEPC showed a more than 20-fold increase in the signal-to-noise ratio as compared to PC microscopy alone (SEPC, 22.2 ± 2.4; PC, 1.0 ± 0.8) (Figure 1c). This indicates that, using SEPC microscopy, AuNPs can be readily discerned from the background while still providing a clear visualization of the underlying cells. Additionally, this suggested that a variety of NPs could be studied using this approach. To further explore which types of nanomaterials can be visualized under SEPC microscopy, we used Lorenz−Mie (LM) theory to establish a framework for predicting the optical response of NPs.

Lorenz−Mie Theory Framework for Nanoparticle Optical Scattering. First reported by Gustav Mie in 1908 in the context of colloidal gold,[23] LM theory is an analytical approach to solving Maxwell's equations for the elastic scattering and absorbance electromagnetic plane waves. Here, we use LM theory as an accessible approach for understanding the optical scattering of ENMs. We note that numerical approaches, such as finite-difference time-domain methods (FDTD), can potentially provide a more accurate model by explicitly incorporating elements of cellular architecture.[24−26] However, these approaches are often time intensive, both to implement and in terms of computational intensity. In contrast, LM theory has been widely reported for a number of different nanomaterials and geometric configurations, such as 1D wires or 2D sheets,[27] and is easily implemented using publicly available software (see the Supporting Information). This allows LM theory the ability to rapidly address a variety of materials, making it a useful metric for initially determining if an ENM will be visible using SEPC microscopy. Under this model, the intensity of scattered light, $I(\lambda)$, is found relative to the illuminating light intensity, $S(\lambda)$, and the dimensionless scattering efficiency, $Q_{sca}(D,\lambda)$, (Figure S3) such that

$$I(\lambda) \propto S(\lambda) \cdot Q_{sca}(D, \lambda) \quad (1)$$

where D is the NP diameter and λ is the wavelength of the illuminating light. As $Q_{sca}(D,\lambda)$ is proportional to the scattered light intensity, it offers a good metric for understanding how bright NPs will appear under DF and, therefore, SEPC microscopy.

Using LM theory, we first calculated the wavelength- and diameter-dependent scattering and absorbance efficiencies, $Q_{abs}(D,\lambda)$ and $Q_{sca}(D,\lambda)$, respectively, of multiple ENMs (Figure 2a), with reference values for the complex refractive index and the extinction coefficients obtained from the literature[28−32] (Figure S4). The metal and metal oxide

DOI: 10.1021/acs.nanolett.8b03903
Nano Lett. 2019, 19, 793−804

particles studied showed strong spectral scattering in the ~300−400 nm range (Figure 2a), with gold showing an additional peak in the visible regime, at 510 nm. In each case, an increase in particle size resulted in an increase in optical scattering intensity and a red-shift in maximal scattering intensity. The exception to this was SiO_2, which showed negligible scattering. To test the validity of LM theory for addressing these materials, the bulk absorbance of AuNPs was measured using UV−vis spectroscopy (Figure S5a), while the spectra of individual particles deposited onto a glass substrate was collected using hyperspectral imaging (Figure 2b). We noted that an increase in particle size was predicted to lead to stronger optical scattering. To avoid biasing our sample toward brighter particles, dimmer background particles were selected for examination under hyperspectral imaging, as these were more likely to reflect the mean particle distribution as indicated by electron microscopy (Figure S5b). In both bulk and single particle scattering, experimental measurements agreed with those values predicted by LM theory (R^2 = 0.91 and R^2 = 0.86, for the bulk absorbance and individual scattering, respectively) (Figure 2b, Figure S5b,c), showing a ~10 nm difference between the predicted and observed spectral peaks, which were likely the result of surface interactions with the underlying substrate. This approach was also used to examine additional ENMs, including Al_2O_3 and CeO_2 NPs (Figure S5d,e), which showed similar matching between predicted and experimental values for individual particle scattering (R^2 = 0.93 and R^2 = 0.90, respectively). Collectively, these data suggest that LM theory is an appropriate model for studying NP scattering.

One key challenge in establishing which materials can be observed using SEPC microscopy is relating the predicted wavelength-dependent scattering coefficients to the observable broadband optical scattering. This requires constructing a weighted optical response, which takes into account the spectrum of the illuminating lamp, the spectral sensitivity of the detector, and the inherent interference of the internal optics. To achieve this, we constructed a normalized wavelength-independent scattering coefficient, $Q_{nsca}(D)$ (Figure S4), using a modified approach for reduction in dimensionality (see the Supporting Information for details), as reported previously for silicon nanowires.[33] This allows for a more direct comparison between the predicted optical scattering and the observed intensity measurements under DF. Using this approach, we calculated $Q_{nsca}(D)$ for a library of metal and metal oxide NPs (Figure 2c). Of the materials surveyed, Ag and Au showed the strongest predicted scattering, while SiO_2 exhibited a negligible response. As this approach in dimensional reduction has not been previously reported in the context of these materials, we wanted to validate that this method offers reasonable experimental predictions. To test this, AuNPs of varying diameters were imaged using DF microscopy under matched optical conditions (0.5−3 s exposures, 50% illuminating power) (Figure S6). The resulting scattering intensities revealed a characteristic curve (Figure S7e), which matched the trend predicted using the normalized scattering coefficients, $Q_{nsca}(D)$ (Figure 2d). This suggested the validity of this approach. Additionally, this allowed for a direct comparison between the predicted and experimentally observed optical scattering, which in turn can be used to establish a threshold scattering intensity.

For NPs to be detected under SEPC, they need to have a higher scattering intensity than the surrounding medium. As adherent cells also scatter a small amount of light, this sets a natural detection threshold, below which it is difficult to distinguish individual particles from the surrounding cell. To determine this detection threshold, AuNPs of varying diameter and HUVECs containing no NPs, were imaged under DF using the same optical conditions (Figure S7a−c). In each case, intensity measurements were then taken as a function of exposure time, with both cells and AuNPs showing a linear response in the relative photon counts (Figure S7d). This allowed us to establish a detection threshold for particle scattering relative to the cells, by enabling a direct comparison between the calculated Q_{nsca} and the corresponding scatter intensity measurement. This yielded normalized scattering coefficients of ~0.010 and ~1.35 for the cell body and the perinuclear regions, respectively. These corresponded to AuNP diameters of 35 and 65 nm, respectively (Figure 2d), suggesting that AuNPs with these diameters or larger can be distinguished from the cell. However, these sizes are material-dependent. For instance, we would not expect SiO_2 particles to be distinguishable from the cell body until ~80 nm in diameter because of their poor scattering coefficients. Additionally, even at 150 nm in diameter, the scattering of SiO_2 particles (Q_{nsca} = 0.125) would be below the level of the perinuclear region. Overall, this creates a theoretical framework for understanding which materials can be tracked using SEPC, as the $Q_{nsca}(D)$ of many materials can readily be determined using LM theory. Finally, we note that while LM theory is most accurate in the case of spherical particles, $Q_{nsca}(D)$ can also be determined for intermediate-sized materials, such as rods and discs, using an FDTD approach, allowing these results to be extended further to more complex geometries.

Confirming ENM Identity. To probe this framework and demonstrate that SEPC microscopy can be applied to a broader range of nanomaterials, a group of metal and metal oxide NPs of varying size and composition were imaged, including Au (18 nm) (Figure 1b), CeO_2 (35 nm), Al_2O_3 (28 nm), Fe_2O_3 (10 and 109 nm diameter), Ag (22 nm), TiO_2 (29 nm), and SiO_2 (15 nm) NPs (Figure S8). These materials were selected as they are among the most commonly produced nanomaterials in a commercial setting,[34,35] making them a point of interest from an environmental exposure perspective. Nanomaterials were synthesized and prepared as previously reported.[36−39] (For a summary of ENMs used here, see Table S2.) Additionally, a control sample containing no nanomaterials was imaged. For those samples containing ENMs, NP suspensions (10 μg/mL) were incubated with HUVECs and imaged using both PC and SEPC microscopy. Among the materials surveyed using LM theory, Ag and Au showed the strongest predicted optical scattering, followed by Al_2O_3, TiO_2, Fe_2O_3, and CeO_2. SiO_2 showed an approximately 2 orders of magnitude reduction in scattering efficiency as compared to other ENMs of a similar diameter (Figure 2c). This matched our experimental findings, as all ENMs surveyed could be detected using SEPC, with the exception of the negative control and those samples exposed to SiO_2, both of which showed a negligible scattering (Figure S8). This suggests that SEPC is amenable to detecting a wide range of material compositions and particle sizes. We note, however, that many of the NPs observed this way were nominally below the detection threshold due to size considerations. As these materials could still be observed, this suggests that NPs were potentially clustering toward aggregates with larger effective cross sections and increased optical scattering. This is

DOI: 10.1021/acs.nanolett.8b03903
Nano Lett. 2019, 19, 793−804

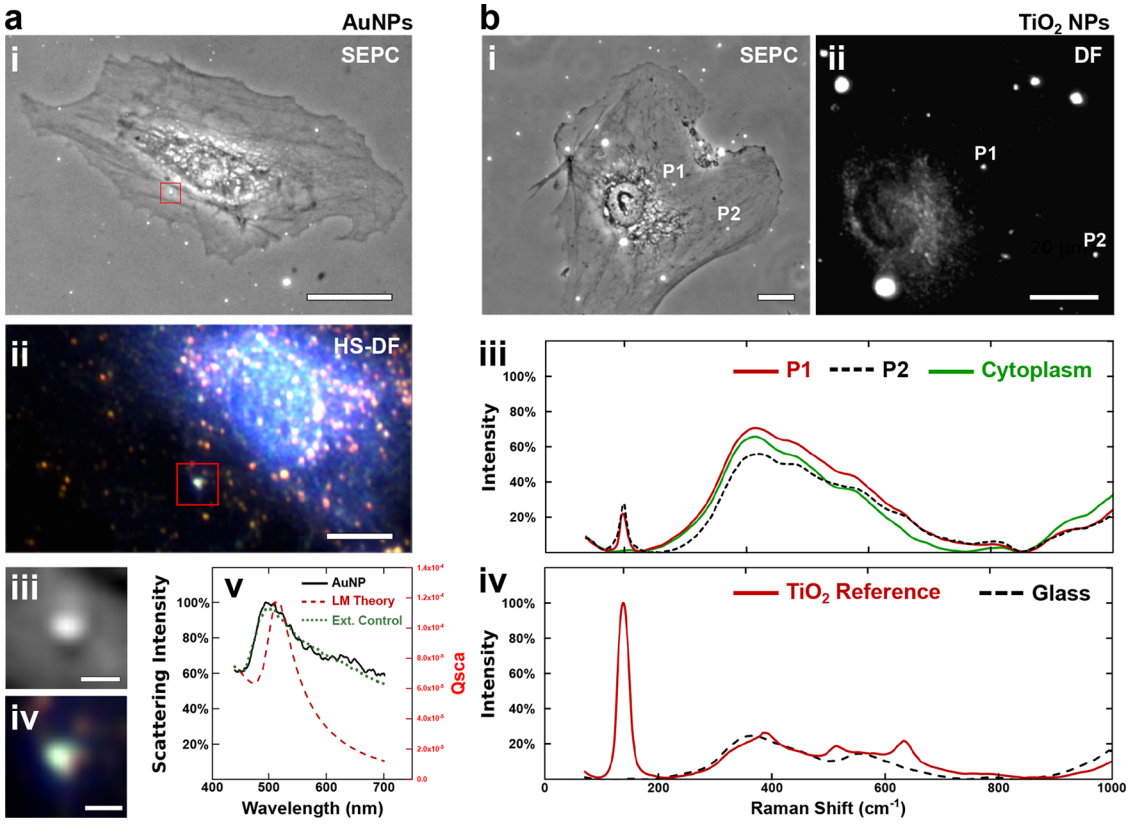

Figure 3. Confirmation of NP identity. To confirm the highlighted objects were NPs and not cellular in origin, integrated hyperspectral darkfield (HS-DF) imaging and Raman spectroscopy were used. Au and TiO_2 NPs were used as controls for their distinct scattering (~520 nm) and Raman (~150 cm^{-1}) peaks, respectively. Representative SEPC image of HUVECs exposed to Au (a, i) and TiO_2 (b, i) NPs (scale bars, 20 μm), with the corresponding hyperspectral micrograph (a, ii) (scale bar, 5 μm) and DF regions (b, ii) (scale bar, 20 μm). (a, iii and iv) High-magnification micrograph showing the particle of interest in SEPC and HS-DF, respectively (scale bars, 1 μm). Inset images were smoothed for clarity. (a, v) Scattering spectrum of the highlighted particles (black) as compared to the average of an external control containing only AuNPs (green), indicating a good match between spectra. (b, iii) Raman spectroscopy further confirmed the ENM identity of the two particles (P1 and P2, red and black) observed under SEPC (b, i), showing a 147 cm^{-1} Raman peak, indicating the presence of TiO_2 as compared to the baseline of a cell (green), an external reference of TiO_2 NPs (red) (b, iv), and a glass substrate containing no ENMs or cells (black).

consistent with previous findings, which indicate that NP endocytosis can lead to particle aggregation.[40]

To study this aggregation phenomenon and confirm the identity of the NPs, hyperspectral imaging and Raman microscopy techniques were used to measure the spectral response of individual particle clusters (Figure 3). While SEPC microscopy is limited in its ability to distinguish multiple nanomaterials from one another, hyperspectral imaging and Raman microscopy can be used to achieve this result, although these systems are difficult to use in a real-time, nondisruptive manner. In each case, ENMs were incubated with HUVECs and imaged using SEPC to identify potential particles of interest. Next, micrographs from the same region were obtained using hyperspectral imaging and Raman microscopy, allowing for a cross-comparison between microscopy techniques. For hyperspectral imaging, AuNPs were selected due to their large characteristic spectral peak in the visible range (Figure 3a), distinguishing them from other metal and metal oxide NPs, which predominately absorb in the ultraviolet region. For reference, an external control containing no cells was also imaged, measuring the spectra of multiple particles to obtain an average spectrum, with images smoothed to reduce shot noise (n = 45). For those particles incubated with HUVECs and observed under SEPC, the spectral response matched the external control, and with the predicted ~520 nm scattering peak (Figure 3a, v). This confirmed the presence of AuNPs, suggesting the fidelity of SEPC for tracking ENM-cell interactions. Additionally, we noted that many of the experimentally observed samples showed a significant red-shift and spectral broadening, reinforcing the idea that particle aggregation was occurring (Figure S9). The identity of the NPs was further confirmed using Raman microscopy. For these experiments, TiO_2 NPs were selected due to their distinct Raman spectra. For both cellular and reference samples containing NPs, a strong 147 cm^{-1} peak was observed (Figure 3b), which is consistent with the previously reported E_g peak of anatase phase titanium oxide.[41] Additionally, this peak was absent from the rest of the cytoplasm and from a blank glass control, containing no cells or NPs. Taken together, these results suggest that the objects visualized under SEPC are the desired ENMs, further indicating that they can be monitored to discern their uptake behavior.

Nanoparticle Transport Dynamics. SEPC microscopy can be used to track real-time particle dynamics, allowing researchers to discriminate between different modes of active cellular transport and ENM uptake (Figure 4). For this study, HUVECs cultured on glass coverslips were exposed to NPs in Tyrode's buffer solution, allowing NPs to deposit onto the cells and the glass substrate, before being swapped into fresh buffer solution. ENM dynamics were then monitored under SEPC for

DOI: 10.1021/acs.nanolett.8b03903
Nano Lett. 2019, 19, 793−804

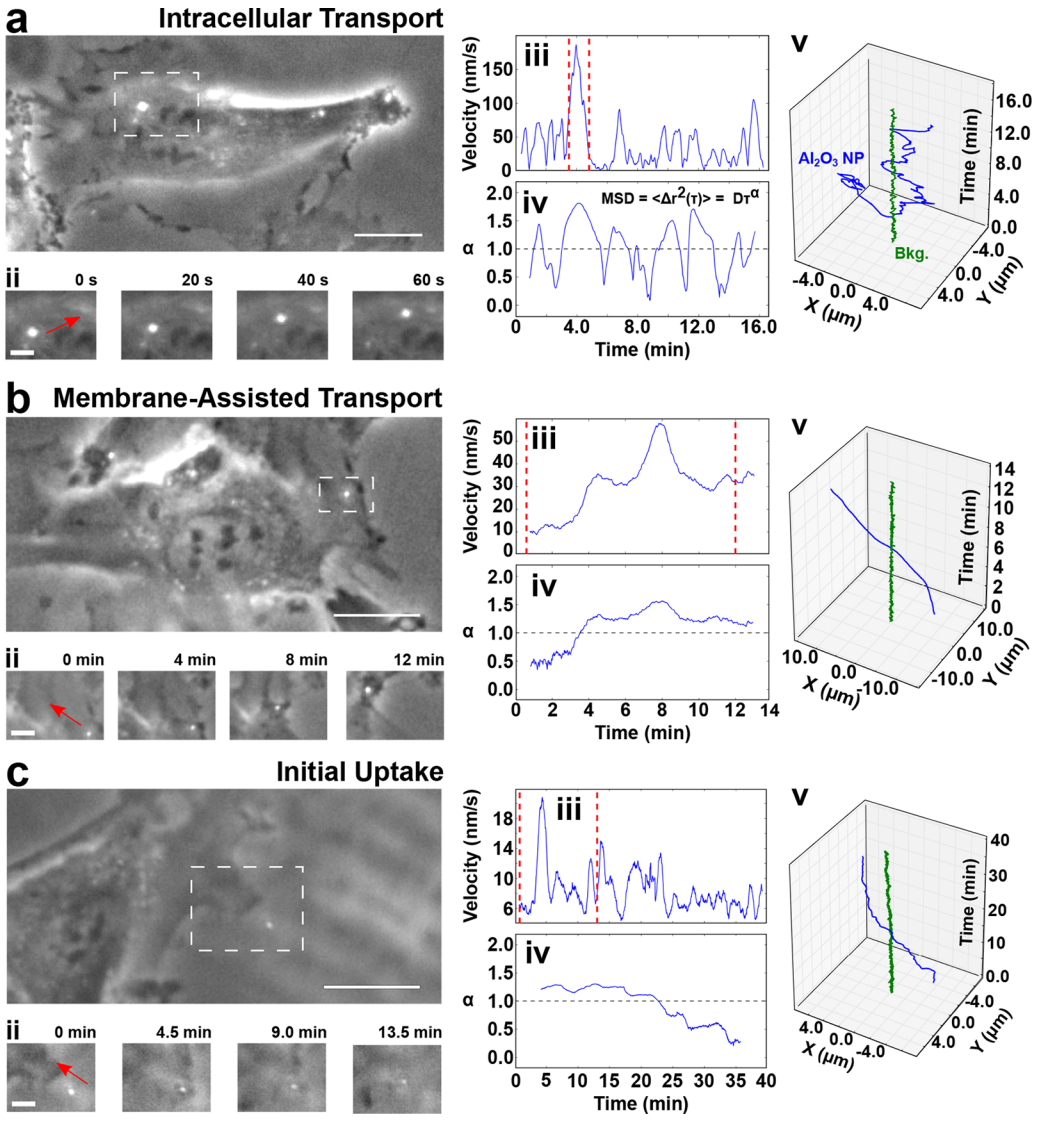

Figure 4. Tracking distinct modes of nanoparticle transport. SEPC can be used to track different modes of aluminum oxide NP transport in cells, including intracellular transport (a), membrane-assisted transport (b), and particle uptake (c). In each case, the particle of interest's transport dynamics (blue) are compared to an external background control particle (green). (i) Example SEPC micrographs showing HUVECs exposed to aluminum oxide NPs, with the corresponding high-magnification inset showing the position of a particle at different time points (ii). NP transport analysis, showing the instantaneous velocity of a particle (iii), mean squared displacement (MSD) coefficient (iv), and path of travel (v), as a function of time. Inset images smoothed for clarity (main-scale bars, 20 μm; inset-scale bars, 5 μm).

2 h, with images acquired at either two or four second intervals. To quantify particle transport, we tracked the particle's path, velocity, and mean squared displacement (MSD), where MSD is the average distance that a particle travels as a function of lag time, given by the following equation:

$$\mathrm{MSD} = \langle \Delta r^2 \rangle = D\tau^{\alpha} \tag{2}$$

with Δr, D, τ, and α representing the particle's displacement, diffusion coefficient, observed lag period, and diffusivity exponent, respectively. Measuring the diffusivity exponent, α, provides insight into the mode of particle transport, with different values indicating restricted diffusion ($\alpha < 1$), Brownian motion ($\alpha = 1$), and active particle transport ($\alpha > 1$). To measure α, a log−log plot of the MSD versus τ was fit using a linear least-squares model, with the slope providing the α value (Figure S10f). To understand the real-time particle dynamics, transport trajectories were segmented using a rolling-time frame analysis (1−3 min). Rather than providing a single α value for the entire particle trajectory, this allowed for changes in the particle transport characteristics to be monitored, as particles often show intermittent periods of stagnation, and quick linear transport, providing a deeper insight into the temporal dynamics.

Tracking the diffusivity exponent, α, revealed several modes of ENM transport. In the case of intracellular transport, we observe short "burst-like" periods as have been previously described[42] (Figure 4a) (Video S1). These were marked by high particle velocities (~200 nm/s in the present case), active diffusivity coefficients ($\alpha > 1$), and linear particle trajectories, with minimal movement of the cell membrane. This type of transport was typically brief relative to the entire acquisition period, lasting ~5 min, and in general showed an overall trajectory toward the perinuclear region. We note that this type of behavior was more consistent with motor-assisted vesicular transport, over cytoplasmic streaming, as the particles

DOI: 10.1021/acs.nanolett.8b03903
Nano Lett. 2019, 19, 793−804

displayed bidirectional movement, back-tracking along their own path (Figure 4a, v). This competition between anterograde and retrograde motion is indicative of assisted transport, suggesting the participation of kinesin and dynein motor proteins.[43] This type of transport was in contrast to other modes, such as membrane-assisted transport and particle uptake, which showed an overall unidirectional motion.

In the case of membrane-assisted transport, particles are carried along by the cell as the membrane deforms (Figure 4b) (Video S2). Using SEPC, we can follow these deformations, allowing us to monitor the cell-ENM interactions simultaneously. This would be difficult to achieve using other real-time tracking methods, such as DF or PC, as these would miss the nanoparticle or membrane component, respectively. In addition to motor protein-assisted transport, movement by the cell membrane is also a form of "active transport" ($\alpha > 1$) as it requires energetic input from the cell. In contrast to other forms of intracellular transport, this mode shows significant membrane deformation and a lower maximum velocity; ∼40−60 nm/s in the present case (Figure 4b, iii). This is consistent with the slower speeds of cell motility, as compared to vesicular transport. Additionally, the time span of membrane-assisted transport was more protracted, occurring over an extended duration (∼12 min in the present case). Similarly, no "burst-like" activity or bidirectional motion was observed in this case, with the particles instead favoring a more constant gradient of motion, progressing steadily in a single direction (Figure 4b, iv and v). This type of motion is also consistent with motility directed transport, as cells change direction on a different time scale than intracellular motor-assisted transport.

Finally, we can also compare both of these types of transport to the initial NP uptake event (Figure 4c) (Video S3). In this case, the NP starts external to the cell, with no initial overlap. The membrane can then be seen to extend out and make contact with the particle (Figure 4c, ii), at which time the particle goes from a stationary to a mobile state. Putting on a brief burst of speed, the particle is brought into the contact with the cell body, where it then becomes relatively quiescent, showing restricted diffusion ($\alpha < 1$), presumed to be awaiting motor-assisted transport to the perinuclear region. Similar to the previously discussed modes of transport, this event also shows periods of active cellular transport ($\alpha > 1$) (Figure 4c, iii); however, it displayed relatively low velocities compared to either membrane- or motor-assisted transport (∼10−20 nm/s). Additionally, similar to the membrane-assisted transport case, the NPs showed a relatively linear motion, with a significant amount of membrane deformation.

The NPs used in the previous example were aluminum oxide; however, this type of tracking can also be extended to work with a range of material compositions and cell types. For instance, here we also demonstrate that the active transport of cerium oxide NPs can be tracked in human aortic smooth muscle cells (HASMCs), showing similar transport dynamics to aluminum oxide (Figure S10) (Video S4). This suggests that SEPC microscopy is applicable to a range of cell types, although in the case of nonadherent spherical cells, large membrane curvatures may make it difficult to distinguish particles from the background scattering. Additionally, we note that while real-time single particle dynamics have been studied for gold,[40] and ensemble studies have been performed for nanoceria[44−46] and alumina[47,48] NPs, this is one of the first reported case of single NP active transport for both nanoceria and alumina. In addition to multiple cell types, this technique can also be used to track a large number of NPs all at once. Here we show the simultaneous tracking of ∼280 TiO_2 NPs (Figure S11) coincubated with HUVECs, undergoing a variety of transport processes, including both initial NP uptake (Figure S11b) and membrane-assisted transport (Figure S11c), with peak speeds of ∼40 nm/s and ∼250 nm/s, respectively. Taken together, this suggests that SEPC can be used to explore a variety of ENM-cell interactions.

Composite Nanoparticle Dynamics. During multi-particle tracking for pleomorphic cells, we noted that there was a spatial heterogeneity in particle transport dynamics within a single cell, where particles could exhibit dissimilar velocities even after similar particle exposure times. This suggests that different regions of the cell may confer distinct transport dynamics. In the pleomorphic case, this effect can be attributed to the influence of cell migration and membrane deformation as revealed by SEPC microscopy, with the lamellipodia traveling at different rates at each end of the cell. However, this makes it difficult to decouple innate transport behavior from cell motility. Even when the membrane remains relatively stationary, variability in membrane morphology means that particles will transverse different distances to reach the perinuclear region. This makes it challenging to normalize transport behavior across multiple cells and multiple NPs. To account for this, we combined SEPC microscopy with microcontact printing to form reproducible cell morphologies. Microcontact printing uses micromolded polydimethylsiloxane (PDMS) stamps to selectively deposit extracellular matrix proteins, forming controllable fibronectin islands (Figure 5a). As cells will preferentially bind to the deposited matrix proteins, this can be used to guide cell shape giving rise to reproducible cell morphologies. Here, we microcontact printed fibronectin islands (2000 μm^2 area) onto PDMS-coated glass coverslips, forming arrays of circular HUVECs (Figure S12). The ability to create reproducible cell islands allows us to normalize NP transport across multiple cells, providing robust data on the temporal dynamics of particle uptake. For this study, we choose to focus on TiO_2 NP uptake, as their brightness and high refractive index make them one of the most abundantly produced nanomaterials, seeing widespread use in inks, pharmaceuticals, food products, and cosmetics.[49] Recently there has been concern over the ability of intravenous TiO_2 particles to transverse biological barriers, showing toxic effects in the brain and liver of developing mice models.[50,51] Understanding the temporal dynamics of nanoparticle uptake can offer potential benefits in controlling and preventing deleterious particle exposure pathways.

Particle uptake was monitored using single-cell islands exposed to 10 $\mu g/mL$ of 100 nm TiO_2 NPs for 10 min, allowing NPs to deposit onto the arrayed islands. After being exchanged into fresh media, samples were then imaged using SEPC microscopy at 20 min intervals. In a representative SEPC micrograph of a single-cell island (Figure 5a), we observe that particles go from being randomly distributed to centrally concentrated over the span of ∼50 min. To quantify this behavior, we superimposed cell micrographs to form a single composite image of NP uptake ($n = 3$ samples, with 24, 32, and 38 cell islands composited for 10, 30, and 50 min, respectively) (Figure 5b). The location of the nucleus was normalized by centrally rotating each micrograph, such that the centroids of the nuclei were registered to the same angle (top-middle, Figure S13). Composite images were then converted

DOI: 10.1021/acs.nanolett.8b03903
Nano Lett. 2019, 19, 793−804

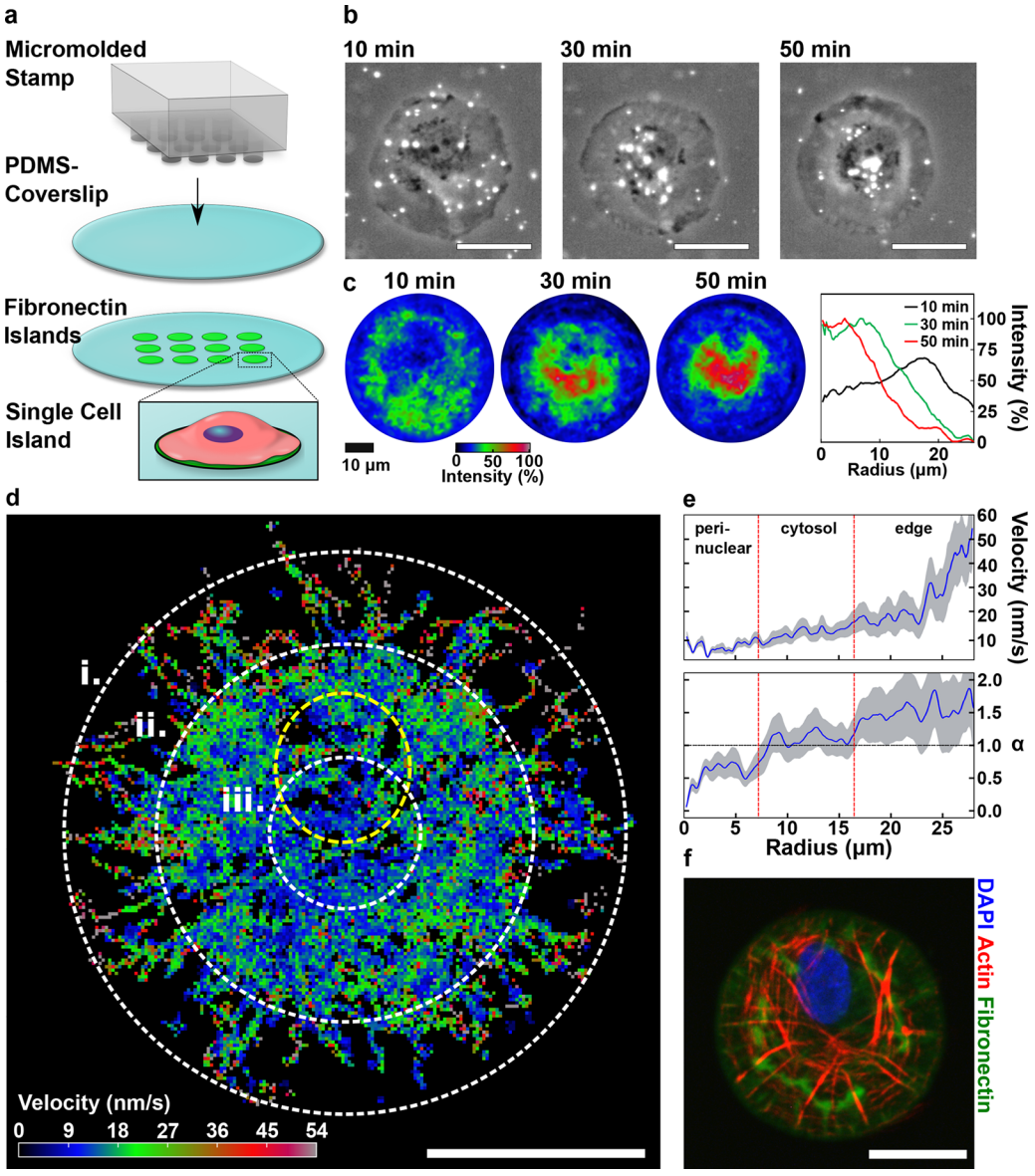

Figure 5. Ensemble nanoparticle dynamics using single-cell composite imaging. (a) PDMS stamps were used to micropattern fibronectin islands (area = 2000 μm^2), yielding reproducible single-cell morphologies. (b) Example SEPC micrographs of HUVEC single-cell islands internalizing TiO_2 nanoparticles (at 10 min, left; 30 min, middle; 50 min, right; scale bars 25 μm). (c) Median 2D intensity measurements of aligned and composited SEPC micrographs (n = 3 samples, 24−38 cell islands each), with the corresponding graph of normalized radial intensity, showing nanoparticle clustering in the perinuclear region as a function of time. (d) Composite of the real-time trajectories of TiO_2 NPs during uptake, showing the average velocity as a function of particle position (n = 12 cells, 3 samples, ~480 nanoparticles, 200 × 200 grid binning, average nucleus position highlighted in yellow, scale bar 20 μm). Perinuclear (i), cytosol (ii), and edge (iii) regions indicated by white highlights. (e) Average radial velocity (upper) and diffusivity exponent (lower) profiles showing region specific transport characteristics (errors bar given as the standard error of the mean, n = 3). (f) Fluorescent micrograph of a single-cell island, showing a radially aligned cytoskeleton (actin = red, fibronectin = green, nucleus = blue; scale bar = 20 μm).

to polar coordinates, and the average intensity was taken as a function of distance from the center of the cell. This allowed for a quantification of the average particle position as a function of time (Figure 5b). Using this approach, we observed that particles began as evenly distributed across the cell, with a maximal intensity at a radius of 17.5 μm from the center. After 30 and 50 min, this was reduced to 6.8 and 4.0 μm, respectively. This indicated that the bulk of nanoparticle transport occurs within the first 30 min of exposure, but that particles showed continued clustering after this point. Additionally, this further supported the idea of a spatial heterogeneity in transport dynamics, as particles showed greater clustering during the initial period, suggesting that particles move faster near the edge of the cell and slow down as they approach the nucleus.

To test this behavior, we measured the ensemble dynamics of TiO_2 NPs during particle uptake. Here, multiple cell islands were monitored in a real-time manner for a period of 50 min at 4 s intervals using SEPC microscopy (n = 3 samples, 12 total cells). Particle trajectories were then extracted as previously described for individual cells (Figure S14a) (Video S5), and composite dynamic maps were constructed by binning the average velocity (Figure 5d) and diffusivity coefficients (Figure S14b) of each particle in a region. Using this composited

DOI: 10.1021/acs.nanolett.8b03903
Nano Lett. 2019, 19, 793−804

approach, we were able to construct a normalized vector map (Video S6) over a plurality of the cell (46.4% area coverage), avoiding potential conflicts of particle overloading and NP indistinguishability in tracking.

Mapping the cell in this manner allowed for a clear visualization of particle dynamics across the cell, revealing three potential regions of interest. First, the edge of the cell appeared to have the highest particle velocities, with the cytosol exhibiting intermediate velocities, and the perinuclear region showing the lowest speeds. To quantify this behavior, the average velocity and diffusion coefficient of the NPs was determined as a function of distance from the centroid (Figure 5d). This showed that particles exhibited a steady decline in transport velocity as they approached the nucleus, with an average velocity of 54 ± 14 nm/s at the outer edges of the cell, down to 6.9 ± 1.6 nm/s in the center. Interestingly, while velocities showed a steady decline, the diffusivity exponent, α, revealed three distinct phases of transport in the cell, with discrete steps beginning at ∼7 μm and ∼17 μm from the center of the cell. We note that these values align well with the peak clustering distances observed previously (Figure 5b). To test whether these regions of particle transport were an artifact of velocity binning, we also examined individual particle trajectories. Similar to the ensemble case, we observed that particles undergo three distinct phases of transport in the cell (Figure S15), transitioning from ∼40 nm/s at the edge of the cell down to a basal velocity of ∼1.2 nm/s. The diffusivity coefficient also showed three distinct regions of transport as observed in the ensemble case. Collectively, this indicated that there are spatial heterogeneities in NP transport dynamics across the cell. To understand this behavior, we looked at the cytoskeletal organization and small perturbations in cellular membrane morphology during ENM exposure.

Because actin filaments serve as an important scaffolding for intracellular vesicle transport, we hypothesized that for particles to cluster in the perinuclear region, actin filaments would also need to converge. Upon fluorescently labeling the actin network, this is indeed what we observe, with labeled cell islands exhibiting radially aligned actin filaments that coincide at a central position (Figure 5f). Additionally, upon comparing the radial projection of the actin filaments and to the composite NP velocities (Figure S14c), we found that both exhibit similar linear alignments, suggesting that the actin filaments helped guide particle clustering in the perinuclear region. We note that such radially aligned chiral actin networks have previously been reported for micropatterned cells,[52] indicating that this is a commonly found motif in cellular architecture. This clustering of the actin filaments suggests a potential explanation for the drop in transport velocities near the perinuclear region. As particles and actin filaments become more densely packed, this results in crowding in the cellular microenvironment, which can lead to a reduction in transport speeds.[53,54] Additionally, as particles near the perinuclear region they can become trapped in lysosomes,[55] resulting in further restricted diffusion. Taken together, this suggests a mechanism for the reduction in NP transport velocities near the perinuclear region.

To probe the mechanism of increased particle transport near the edge of the cell, we used SEPC microscopy to measure local cellular membrane deformations. As lamellipodia protrusions and retractions have been shown to regulate retrograde flows,[56] we reasoned that this process could also be impacting NP transport. While microcontact printing results in normalized cell shapes, this does so by forming focal adhesion complexes with the underlying extracellular matrix proteins.[57] As a result, some cells are still able to extend their lamellipodia past the fibronectin island by expanding their actin network, creating small changes in local membrane curvature. To measure these deviations in the lamellipodia, we used SEPC microscopy, which revealed an ∼10 μm region of membrane instability (Figure S16). This corresponded well with the observed region of increased activity near the edge of the cell, Additionally, NPs exhibited similar transport velocities compared to those reported for membrane protrusion (54 ± 14 nm/s for NPs compared to ∼50 nm/s for retrograde flow).[56] Collectively, this suggests that NP transport is regulated by membrane dynamics in this region of the cell.

Overall, this highlights the important role that membrane dynamics has in NP transport. For both pleomorphic and microcontact printed cells, we observed membrane-dependent effects. In the pleomorphic case, we observed distinct differences between membrane-assisted transport and other modes of active transport, while for microcontact printed cells we observed that membrane instabilities can potentiate retrograde flow. The ability of SEPC microscopy to track both NPs and cells simultaneously allowed us to resolve these behaviors, which can be difficult to achieve when tracking NPs alone. As a result, this work suggests that membrane dynamics play a larger role in nanoparticle uptake and transport then has been previously reported.

Conclusion. Here, we have shown that SEPC microscopy can be used as a generalized approach for studying label-free nanomaterial uptake, offering insights into spatial heterogeneity in NP transport. In the present study, we have limited our approach to metals and metal oxides as these are among the most commonly used materials in a commercial setting. However, we also believe that this technique has potential implications for a much wider range of emerging materials, such as polymeric materials, which are routinely studied using optical scattering approaches. To supplement this, we have shown that Lorenz−Mie theory can be used to predict the optical scattering properties of nanoparticles, providing a framework for understanding which materials can be tracked using SEPC microscopy. We were able to achieve this by introducing a normalized wavelength-independent scattering coefficient, $Q_{nsca}(D)$, which allowed us to directly relate predicted scattering coefficients to experimentally observed optical intensities. This indicated that SEPC could be used to distinguish nanoparticles down to ∼35 nm in size. We then used SEPC microscopy to track different modes of active transport in both pleomorphic and microcontact printed cells. In each case, the ability of SEPC microscopy to simultaneously track both nanoparticles and cell membranes offered key insights into nanoparticle uptake dynamics.

As a label-free approach, SEPC has the potential to address several key challenges in the field. First, SEPC microscopy can be used to explore the impact of surface modification on nanoparticle uptake. While this has been studied for labeled materials,[58] it has previously been difficult to compare these results to label-free control. In this way, SEPC allows for a rational exploration of nanomaterial surface properties and their role in endocytosis and cellular transport. Second, this technique has the potential to offer new insights into endosomal escape and nanomaterial exocytosis pathways. Research to date has primarily focused on initial nanoparticle uptake mechanisms;[40,59] however, little is known about the

DOI: 10.1021/acs.nanolett.8b03903
Nano Lett. 2019, 19, 793−804

long-term fate of intracellular particles.[59] This is in part due to a reliance on fluorescent labels for nanoparticle tracking, which can break down in the harsh environment of the lysosome. This limits the lifetime of fluorescence-based uptake and distribution studies. Using SEPC microscopy, it should be possible to continue tracking nanoparticle activity after this critical juncture, potentially offering new insight into these less understood pathways. Collectively, this suggests that SEPC has important implications for designing next-generation nanoparticle-based drug delivery systems and in better understanding the cellular interactions of existing nanomaterials.

Methods. For cell culture, HUVECs were maintained under sterile conditions at 37 °C and 5% CO_2, using Medium 200 (Gibco) with the corresponding low serum endothelial growth supplement (LSGS, Thermo Fischer Scientific), which contains fetal bovine serum (2% v/v), hydrocortisone (1 μg/mL), human epidermal growth factor (10 ng/mL), basic fibroblast growth factor (3 ng/mL), and heparin (10 μg/mL). All cells used were between passage four and nine, with media exchange after 24 h and every 48 h thereafter.

Scatter Enhanced Phase Contrast Microscopy. To simultaneously track cells and nanomaterials using SEPC, an Olympus ix83 inverted microscope, with a phase contrast plate, was retrofitted with an oblique angle LED ring illuminator (Amscope LED-144-YK ring lamp), which attached to the microscopes brightfield condenser. Using this ring LED setup, we were able to achieve longer condenser (~3 cm) working distances as compared to traditional setups, which take the place of the brightfield condenser. Typical LED powers were between 20 and 50% of maximum power (Figure S6).

For phase contrast microscopy, LUCPlanFLNPh 20× and 40× objectives were used. with a numerical aperture (NA) of 0.4 and 0.65, respectively. The relatively low NA cut down on background scattering allows for a clear DF image. For live cell imaging, an Air-Therm ATX-H thermal heater coupled to a Precision Plastics stage top incubator was employed, maintaining physiological conditions (i.e., 95% humidity, 37 °C internal temperatures, pH = 7.4).

Images were recorded on a Hamamatsu Orca Flash 4.0 C11440 at a 16 bit depth with a 0.16−0.33 μm pixel resolution.

■ ASSOCIATED CONTENT

Supporting Information

The Supporting Information is available free of charge on the ACS Publications website at DOI: 10.1021/acs.nanolett.8b03903.

Experimental methods for hyperspectral imaging and Raman spectroscopy, oblique angle luminosity measurements, UV−vis absorption spectroscopy, sample preparation for transmission electron microscopy, nanomaterial synthesis and dispersion, particle transport dynamics, Lorenz−Mie theory calculations, statistical analysis and signal-noise ratio measurements, microcontact printing, composite nanoparticle dynamics, comparison of cell and nanoparticle imaging modalities, gold nanoparticle diameter characterization, schematic diagram of nanoparticle optical scattering, example work flow for calculating the normalized scattering coefficients, comparison of Lorenz−Mie theory to bulk experimental measurements, oblique angle ring illuminator intensity, comparative measurements of AuNP and HUVECs scattering intensities, SEPC as a generalized approach for imaging nanomaterials, particle aggregation analysis, example of active transport of cerium oxide particles in HASMCs, simultaneous tracking of multiple titanium dioxide nanoparticles in HUVECs, microcontact printing can be used to create reproducible arrays of single-cell islands, average nucleus positioning, mapping composite particle trajectories, single particle transport in microcontact printed islands, dynamic membrane instability, reference sources used for determining the wavelength-dependent refractive index of the reference materials, morphological and structural properties of Au nanoparticles, chemical and biological properties of Ag ENMs, and video descriptions (PDF)

Video S1 (AVI)

Video S2 (AVI)

Video S3 (AVI)

Video S4 (AVI)

Video S5 (AVI)

Video S6 (AVI)

■ AUTHOR INFORMATION

Corresponding Author

*E-mail: kkparker@seas.harvard.edu. Fax: +(617) 495-9837. Tel: +(617) 495-2850.

ORCID

Kevin Kit Parker: 0000-0002-5968-7535

Author Contributions

K.K.P. supervised the research. K.K.P., J.F.Z., and H.A.M.A. designed the study. J.F.Z. and H.A.M.A. performed the experiments. J.F.Z. and H.A.M.A. analyzed the data. G.P. and J.D. synthesized the ENMs and characterized their composition. B.M. and P.D. supervised the synthesis and characterization of the ENMs. All authors discussed the results and contributed to the writing of the final manuscript.

Notes

The authors declare no competing financial interest.

■ ACKNOWLEDGMENTS

We thank Dr. Arthur McClelland for the technical assistance for instrument usage and data analysis for hyperspectral and Raman imaging. Additionally, we thank S. Kim for graciously providing PDMS stamps for microcontact printing. This work was partially supported by the Wyss Institute for Biologically Inspired Engineering at Harvard University. For the characterization nanoparticles using a hyperspectral darkfield Raman microscope, we thank the Harvard Center for Nanoscale Systems (CNS), which is a member of the National Nanotechnology Infrastructure Network (NNIN) under NSF award no. 1541959. This work was performed in part at the Harvard MRSEC (grant no. DMR-1420570). Research reported in this publication was supported by National Institute of Environmental Health Sciences (NIEHS) of the National Institutes of Health (NIH grant no. U01ES027272) as part of the Nanotechnology Health Implications Research (NHIR) Consortium. J.F.Z. acknowledges support from Harvard University and by the Organ Design and Engineering Postdoctoral Training (ODET) program through Brigham and Women's Hospital, National Institute of Biomedical Imaging and Bioengineering (NIBIB), and the National Institute of Health under award no. 5-T32-EB016652-04. H.A.M.A. would like to thank the American Chemical Society for generous support through the Irving S. Sigal Postdoctoral Fellowship.

DOI: 10.1021/acs.nanolett.8b03903
Nano Lett. 2019, 19, 793−804

The content is solely the responsibility of the authors and does not necessarily represent the official views of the National Institutes of Health. The engineered nanomaterials used in the research presented in this publication have been procured or synthesized and characterized by the Engineered Nanomaterials Resource and Coordination Core (ERCC) at the Center for Nanotechnology and Nanotoxicology at Harvard School of Public Health, part of the NIEHS/NHIR consortium.

■ ABBREVIATIONS

SEPC, scatter enhanced phase contrast; HUVECs, human umbilical vascular endothelial cells; HASMCs, human aortic smooth muscle cells; ENMs, engineered nanomaterials; DLS, dynamic light scattering; DF, darkfield microscopy; PC, phase contrast microscopy; NP, nanoparticle; HS-DF, hyperspectral darkfield imaging; LM theory, Lorenz−Mie theory; PDMS, polydimethylsiloxane

■ REFERENCES

(1) Whitesides, G. M. The "right" Size in Nanobiotechnology. *Nat. Biotechnol.* **2003**, *21* (10), 1161−1165.
(2) Nel, A. E.; Mädler, L.; Velegol, D.; Xia, T.; Hoek, E. M. V.; Somasundaran, P.; Klaessig, F.; Castranova, V.; Thompson, M. Understanding Biophysicochemical Interactions at the Nano-Bio Interface. *Nat. Mater.* **2009**, *8* (7), 543−557.
(3) Summers, H. D.; Rees, P.; Holton, M. D.; Brown, M. R.; Chappell, S. C.; Smith, P. J.; Errington, R. J. Statistical Analysis of Nanoparticle Dosing in a Dynamic Cellular System. *Nat. Nanotechnol.* **2011**, *6* (3), 170−174.
(4) Ferrari, M. Cancer Nanotechnology: Opportunities and Challenges. *Nat. Rev. Cancer* **2005**, *5* (3), 161−171.
(5) Korin, N.; Kanapathipillai, M.; Matthews, B. D.; Crescente, M.; Brill, A.; Mammoto, T.; Ghosh, K.; Jurek, S.; Bencherif, S. A.; Bhatta, D.; et al. Shear-Activated Nanotherapeutics for Drug Targeting to Obstructed Blood Vessels. *Science (Washington, DC, U. S.)* **2012**, *337* (6095), 738−742.
(6) Parameswaran, R.; Carvalho-de-Souza, J. L.; Jiang, Y.; Burke, M. J.; Zimmerman, J. F.; Koehler, K.; Phillips, A. W.; Yi, J.; Adams, E. J.; Bezanilla, F. Photoelectrochemical Modulation of Neuronal Activity with Free-Standing Coaxial Silicon Nanowires. *Nat. Nanotechnol.* **2018**, *393a*, 260.
(7) Mayor, S.; Pagano, R. E. Pathways of Clathrin-Independent Endocytosis. *Nat. Rev. Mol. Cell Biol.* **2007**, *8* (8), 603−612.
(8) Harush-Frenkel, O.; Debotton, N.; Benita, S.; Altschuler, Y. Targeting of Nanoparticles to the Clathrin-Mediated Endocytic Pathway. *Biochem. Biophys. Res. Commun.* **2007**, *353* (1), 26−32.
(9) Chithrani, B. D.; Chan, W. C. W. Elucidating the Mechanism of Cellular Uptake and Removal of Protein-Coated Gold Nanoparticles of Different Sizes and Shapes. *Nano Lett.* **2007**, *7* (6), 1542−1550.
(10) Gratton, S. E. a.; Ropp, P. a.; Pohlhaus, P. D.; Luft, J. C.; Madden, V. J.; Napier, M. E.; DeSimone, J. M. The Effect of Particle Design on Cellular Internalization Pathways. *Proc. Natl. Acad. Sci. U. S. A.* **2008**, *105* (33), 11613−11618.
(11) Jiang, X.; Röcker, C.; Hafner, M.; Brandholt, S.; Dörlich, R. M.; Nienhaus, G. U. Endo- and Exocytosis of Zwitterionic Quantum Dot Nanoparticles by Live HeLa Cells. *ACS Nano* **2010**, *4* (11), 6787−6797.
(12) Hillaireau, H.; Couvreur, P. Nanocarriers' Entry into the Cell: Relevance to Drug Delivery. *Cell. Mol. Life Sci.* **2009**, *66* (17), 2873−2896.
(13) Chou, L. Y. T.; Ming, K.; Chan, W. C. W. Strategies for the Intracellular Delivery of Nanoparticles. *Chem. Soc. Rev.* **2011**, *40* (1), 233−245.
(14) Jiang, W.; Kim, B. Y. S.; Rutka, J. T.; Chan, W. C. W. Nanoparticle-Mediated Cellular Response Is Size-Dependent. *Nat. Nanotechnol.* **2008**, *3* (3), 145−150.
(15) Agarwal, R.; Singh, V.; Jurney, P.; Shi, L.; Sreenivasan, S. V.; Roy, K. Mammalian Cells Preferentially Internalize Hydrogel Nanodiscs over Nanorods and Use Shape-Specific Uptake Mechanisms. *Proc. Natl. Acad. Sci. U. S. A.* **2013**, *110* (43), 17247−17252.
(16) Lesniak, A.; Fenaroli, F.; Monopoli, M. P.; Åberg, C.; Dawson, K. a.; Salvati, A. Effects of the Presence or Absence of a Protein Corona on Silica Nanoparticle Uptake and Impact on Cells. *ACS Nano* **2012**, *6* (7), 5845−5857.
(17) Chithrani, B. D.; Chan, W. C. W. Elucidating the Mechanism of Cellular Uptake and Removal of Protein-Coated Gold Nanoparticles of Different Sizes and Shapes. *Nano Lett.* **2007**, *7* (6), 1542−1550.
(18) Panariti, A.; Miserocchi, G.; Rivolta, I. The Effect of Nanoparticle Uptake on Cellular Behavior: Disrupting or Enabling Functions? *Nanotechnol., Sci. Appl.* **2012**, *5* (1), 87−100.
(19) Gratton, S. E. a.; Ropp, P. a.; Pohlhaus, P. D.; Luft, J. C.; Madden, V. J.; Napier, M. E.; DeSimone, J. M. The Effect of Particle Design on Cellular Internalization Pathways. *Proc. Natl. Acad. Sci. U. S. A.* **2008**, *105* (33), 11613−11618.
(20) Tenzer, S.; Docter, D.; Kuharev, J.; Musyanovych, A.; Fetz, V.; Hecht, R.; Schlenk, F.; Fischer, D.; Kiouptsi, K.; Reinhardt, C.; et al. Rapid Formation of Plasma Protein Corona Critically Affects Nanoparticle Pathophysiology. *Nat. Nanotechnol.* **2013**, *8* (10), 772−781.
(21) Walser, T.; Limbach, L. K.; Brogioli, R.; Erismann, E.; Flamigni, L.; Hattendorf, B.; Juchli, M.; Krumeich, F.; Ludwig, C.; Prikopsky, K.; et al. Persistence of Engineered Nanoparticles in a Municipal Solid-Waste Incineration Plant. *Nat. Nanotechnol.* **2012**, *7* (8), 520−524.
(22) Zimmerman, J. F.; Murray, G. F.; Wang, Y.; Jumper, J. M.; Austin, J. R.; Tian, B. Free-Standing Kinked Silicon Nanowires for Probing Inter- and Intracellular Force Dynamics. *Nano Lett.* **2015**, *15* (8), 5492−5498.
(23) Mie, G. Beiträge Zur Optik Trüber Medien, Speziell Kolloidaler Metallösungen. *Ann. Phys.* **1908**, *330* (3), 377−445.
(24) Tanev, S.; Sun, W.; Pond, J.; Tuchin, V. V.; Zharov, V. P. Flow Cytometry with Gold Nanoparticles and Their Clusters as Scattering Contrast Agents: FDTD Simulation of Light-Cell Interaction. *J. Biophotonics* **2009**, *2* (8−9), 505−520.
(25) Myroshnychenko, V.; Rodríguez-Fernández, J.; Pastoriza-Santos, I.; Funston, A. M.; Novo, C.; Mulvaney, P.; Liz-Marzán, L. M.; García de Abajo, F. J. Modelling the Optical Response of Gold Nanoparticles. *Chem. Soc. Rev.* **2008**, *37* (9), 1792.
(26) Gallinet, B.; Butet, J.; Martin, O. J. F. Numerical Methods for Nanophotonics: Standard Problems and Future Challenges. *Laser Photon. Rev.* **2015**, *9* (6), 577−603.
(27) Bohren, C. F.; Huffman, D. R.; Bohren, C. F.; Huffman, D. R. *Absorption and Scattering of Light by Small Particles* **2007**, 1.
(28) Johnson, P. B.; Christy, R. W. Optical Constants of the Noble Metals. *Phys. Rev. B* **1972**, *6* (12), 4370−4379.
(29) Patsalas, P.; Logothetidis, S.; Metaxa, C. Optical Performance of Nanocrystalline Transparent Ceria Films. *Appl. Phys. Lett.* **2002**, *81* (3), 466−468.
(30) Querry, M. R. *Optical Constants of Minerals and Other Materials from the Millimeter to the Ultraviolet; Military Contractor Report No. AD-A158 623*; University of Missouri: Kansas City, MO, 1985.
(31) Gao, L.; Lemarchand, F.; Lequime, M. Refractive Index Determination of SiO2 Layer in the UV/Vis/NIR Range: Spectrophotometric Reverse Engineering on Single and Bi-Layer Designs. *J. Eur. Opt. Soc. Rapid Publ.* **2013**, *8*, 13010.
(32) Siefke, T.; Kroker, S.; Pfeiffer, K.; Puffky, O.; Dietrich, K.; Franta, D.; Ohlídal, I.; Szeghalmi, A.; Kley, E.-B.; Tünnermann, A. Materials Pushing the Application Limits of Wire Grid Polarizers Further into the Deep Ultraviolet Spectral Range. *Adv. Opt. Mater.* **2016**, *4* (11), 1780−1786.
(33) Zimmerman, J. F.; Murray, G. F.; Tian, B. Optical Determination of Silicon Nanowire Diameters for Intracellular Applications. *J. Phys. Chem. C* **2015**, *119* (52), 29105−29115.
(34) Hendren, C. O.; Mesnard, X.; Dröge, J.; Wiesner, M. R. Estimating Production Data for Five Engineered Nanomaterials As a

DOI: 10.1021/acs.nanolett.8b03903
Nano Lett. 2019, 19, 793−804

Basis for Exposure Assessment. *Environ. Sci. Technol.* **2011**, *45* (7), 2562−2569.
(35) Piccinno, F.; Gottschalk, F.; Seeger, S.; Nowack, B. Industrial Production Quantities and Uses of Ten Engineered Nanomaterials in Europe and the World. *J. Nanopart. Res.* **2012**, *14* (9), 1109 DOI: 10.1007/s11051-012-1109-9.
(36) Beltran-Huarac, J.; Zhang, Z.; Pyrgiotakis, G.; DeLoid, G.; Vaze, N.; Demokritou, P. Development of Reference Metal and Metal Oxide Engineered Nanomaterials for Nanotoxicology Research Using High Throughput and Precision Flame Spray Synthesis Approaches. *NanoImpact* **2018**, *10*, 26−37.
(37) Ahn, S.; Ardoña, H. A. M.; Lind, J. U.; Eweje, F.; Kim, S. L.; Gonzalez, G. M.; Liu, Q.; Zimmerman, J. F.; Pyrgiotakis, G.; Zhang, Z.; et al. Mussel-Inspired 3D Fiber Scaffolds for Heart-on-a-Chip Toxicity Studies of Engineered Nanomaterials. *Anal. Bioanal. Chem.* **2018**, *410*, 6141.
(38) DeLoid, G. M.; Cohen, J. M.; Pyrgiotakis, G.; Demokritou, P. Preparation, Characterization, and in Vitro Dosimetry of Dispersed, Engineered Nanomaterials. *Nat. Protoc.* **2017**, *12* (2), 355−371.
(39) Taurozzi, J. S.; Hackley, V. A.; Wiesner, M. R. Ultrasonic Dispersion of Nanoparticles for Environmental, Health and Safety Assessment − Issues and Recommendations. *Nanotoxicology* **2011**, *5* (4), 711−729.
(40) Liu, M.; Li, Q.; Liang, L.; Li, J.; Wang, K.; Li, J.; Lv, M.; Chen, N.; Song, H.; Lee, J. Real-Time Visualization of Clustering and Intracellular Transport of Gold Nanoparticles by Correlative Imaging. *Nat. Commun.* **2017**, *8*, 1−10.
(41) Balachandran, U.; Eror, N. G. Raman Spectra of Titanium Dioxide. *J. Solid State Chem.* **1982**, *42* (3), 276−282.
(42) Wang, B.; Kuo, J.; Granick, S. Bursts of Active Transport in Living Cells. *Phys. Rev. Lett.* **2013**, *111* (20), 208102.
(43) Welte, M. A. Bidirectional Transport along Microtubules. *Curr. Biol.* **2004**, *14* (13), R525−R537.
(44) Vassie, J. A.; Whitelock, J. M.; Lord, M. S. Endocytosis of Cerium Oxide Nanoparticles and Modulation of Reactive Oxygen Species in Human Ovarian and Colon Cancer Cells. *Acta Biomater.* **2017**, *50*, 127−141.
(45) Das, S.; Dowding, J. M.; Klump, K. E.; Mcginnis, J. F.; Self, W.; Seal, S. Cerium Oxide Nanoparticles : Applications and Prospects in Nanomedicine. *Nanomedicine* **2013**, *8* (9), 1483−1508.
(46) Singh, S.; Kumar, A.; Karakoti, A.; Seal, S.; Self, W. T. Unveiling the Mechanism of Uptake and Sub-Cellular Distribution of Cerium Oxide Nanoparticles. *Mol. BioSyst.* **2010**, *6* (10), 1813.
(47) Park, E. J.; Lee, G. H.; Yoon, C.; Jeong, U.; Kim, Y.; Cho, M. H.; Kim, D. W. Biodistribution and Toxicity of Spherical Aluminum Oxide Nanoparticles. *J. Appl. Toxicol.* **2016**, *36* (3), 424−433.
(48) Wagner, A. J.; Bleckmann, C. A.; Murdock, R. C.; Schrand, A. M.; Schlager, J. J.; Hussain, S. M. Cellular Interaction of Different Forms of Aluminum Nanoparticles in Rat Alveolar Macrophages. *J. Phys. Chem. B* **2007**, *111* (25), 7353−7359.
(49) Shi, H.; Magaye, R.; Castranova, V.; Zhao, J. Titanium Dioxide Nanoparticles: A Review of Current Toxicological Data. *Part. Fibre Toxicol.* **2013**, *10* (1), 15.
(50) Jia, X.; Wang, S.; Zhou, L.; Sun, L. The Potential Liver, Brain, and Embryo Toxicity of Titanium Dioxide Nanoparticles on Mice. *Nanoscale Res. Lett.* **2017**, *12* (1), 478.
(51) Yamashita, K.; Yoshioka, Y.; Higashisaka, K.; Mimura, K.; Morishita, Y.; Nozaki, M.; Yoshida, T.; Ogura, T.; Nabeshi, H.; Nagano, K.; et al. Silica and Titanium Dioxide Nanoparticles Cause Pregnancy Complications in Mice. *Nat. Nanotechnol.* **2011**, *6* (5), 321−328.
(52) Tee, Y. H.; Shemesh, T.; Thiagarajan, V.; Hariadi, R. F.; Anderson, K. L.; Page, C.; Volkmann, N.; Hanein, D.; Sivaramakrishnan, S.; Kozlov, M. M.; et al. Cellular Chirality Arising from the Self-Organization of the Actin Cytoskeleton. *Nat. Cell Biol.* **2015**, *17* (4), 445−457.
(53) Engelke, H.; Heinrich, D.; Rädler, J. O. Probing GFP-Actin Diffusion in Living Cells Using Fluorescence Correlation Spectroscopy. *Phys. Biol.* **2010**, *7* (4), 046014.
(54) Höfling, F.; Franosch, T. Anomalous Transport in the Crowded World of Biological Cells. *Rep. Prog. Phys.* **2013**, *76* (4), 046602.
(55) Behzadi, S.; Serpooshan, V.; Tao, W.; Hamaly, M. A.; Alkawareek, M. Y.; Dreaden, E. C.; Brown, D.; Alkilany, A. M.; Farokhzad, O. C.; Mahmoudi, M. Cellular Uptake of Nanoparticles: Journey inside the Cell. *Chem. Soc. Rev.* **2017**, *46* (14), 4218−4244.
(56) Vitriol, E. A.; Wise, A. L.; Berginski, M. E.; Bamburg, J. R.; Zheng, J. Q. Instantaneous Inactivation of Cofilin Reveals Its Function of F-Actin Disassembly in Lamellipodia. *Mol. Biol. Cell* **2013**, *24* (14), 2238−2247.
(57) Grosberg, A.; Kuo, P.-L.; Guo, C.-L.; Geisse, N. a.; Bray, M.-A.; Adams, W. J.; Sheehy, S. P.; Parker, K. K. Self-Organization of Muscle Cell Structure and Function. *PLoS Comput. Biol.* **2011**, *7* (2), No. e1001088.
(58) Wong, M. H.; Misra, R. P.; Giraldo, J. P.; Kwak, S. Y.; Son, Y.; Landry, M. P.; Swan, J. W.; Blankschtein, D.; Strano, M. S. Lipid Exchange Envelope Penetration (LEEP) of Nanoparticles for Plant Engineering: A Universal Localization Mechanism. *Nano Lett.* **2016**, *16* (2), 1161−1172.
(59) Park, J. H.; Oh, N. Endocytosis and Exocytosis of Nanoparticles in Mammalian Cells. *Int. J. Nanomed.* **2014**, *9*, 51.

DOI: 10.1021/acs.nanolett.8b03903
Nano Lett. 2019, 19, 793−804